Chapter 4
Airfoil Shape Optimization Using Variable-Fidelity Modeling and Shape-Preserving Response Prediction

Slawomir Koziel and Leifur Leifsson

Abstract. Shape optimization of airfoils is of primary importance in the design of aircraft and turbomachinery with computational fluid dynamic (CFD) being the major design tool. However, as CFD simulation of the fluid flow past airfoils is computationally expensive, and numerical optimization often requires a large number of simulations with several design variables, direct optimization may not be practical. This chapter describes a computationally efficient and robust methodology for airfoil design. The presented approach replaces the direct optimization of an accurate but computationally expensive high-fidelity airfoil model by an iterative re-optimization of a corrected low-fidelity model. The shape-preserving response prediction technique is utilized to correct the low-fidelity model by aligning the pressure and skin friction distributions of the low-fidelity model with the corresponding distributions of the high-fidelity model. The algorithm requires one evaluation of the high-fidelity CFD model per design iteration. The algorithm is applied to several example case studies at both transonic and high-lift flow conditions.

4.1 Introduction

The use of optimization methods in the design process, as a design support tool or for design automation, has now become commonplace. In aircraft design, the development of numerical optimization techniques started in the mid 1970's when Hicks and Henne [1] used gradient-based optimization methods coupled with computational fluid dynamic (CFD) codes to design airfoils and wings at both

Slawomir Koziel · Leifur Leifsson
Engineering Optimization & Modeling Center,
School of Science and Engineering, Reykjavik University,
Menntavegur 1, Reykjavik, Iceland
email: koziel@ru.is, leifurth@ru.is

X.-S. Yang & S. Koziel (Eds.): Computational Optimization & Applications, SCI 359, pp. 99–124.
springerlink.com © Springer-Verlag Berlin Heidelberg 2011

subsonic and transonic conditions. Substantial progress in gradient-based methods for aerodynamic design has been made since then. Jameson [2] introduced control theory and continuous adjoint methods to the optimal aerodynamic design for two-dimensional airfoils and three-dimensional wings. Initially, using inviscid flow solvers [3, 4], and later using viscous flow solvers [5, 6].

The use of higher fidelity methods, coupled with optimization techniques, has led to improved design efficiency. However, simulation-driven aerodynamic design optimization involves numerous challenges. In particular, the high-fidelity CFD simulations are computationally expensive (e.g., three-dimensional simulations of turbulent flows can take many days on a parallel computer), the design optimization normally requires a large number of simulations, and a large number of design variables are often involved. Therefore, direct optimization of the high-fidelity CFD model may be impractical, especially when using traditional gradient-based techniques.

Computationally feasible design exploiting CFD simulations can be realized using surrogate-based optimization (SBO) techniques [7, 8]. One of the objectives of SBO is to reduce the number of evaluations of the high-fidelity models, and thereby making the optimization process more efficient. This is achieved by using computationally cheap surrogate functions in lieu of the CPU-intensive high-fidelity models. The surrogate models can be created either by approximating the sampled high-fidelity model data using regression (so-called function-approximation surrogates), or by correcting physics-based low-fidelity models which are less accurate but computationally cheap representations of the high-fidelity models.

A variety of techniques are available to create the function-approximation surrogate model, such as polynomial regression [7] and kriging [9]. Function-approximation models are versatile, however, they normally require substantial amount of data samples to ensure good accuracy. The physics-based surrogates are constructed by correcting the underlying low-fidelity models, which can be obtained through simplified physics models [10], coarse-discretization CFD simulation [11], or relaxed convergence criteria [12]. Popular correction methods include response correction [13] and space mapping [14].

The physics-based surrogate models are typically more expensive to evaluate than the function-approximation surrogates, but less high-fidelity model data is needed to obtain a given accuracy level. In many cases, SBO algorithms that utilize physics-based low-fidelity models—so-called variable- or multi-fidelity SBO—typically require only a single high-fidelity model evaluation per algorithm iteration. Due to this, the variable-fidelity SBO method is more scalable to larger numbers of design variables (assuming that no derivative information is required). A review of SBO methods popular in aerospace design can be found in [7] and [8].

In this chapter we describe a computationally efficient variable-fidelity airfoil shape optimization methodology [15, 16, 17], which employs physics-based low-fidelity surrogate models created by means of the shape-preserving response prediction (SPRP) technique [18]. Section 4.2 describes briefly the problem formulation for airfoil shape optimization. The optimization methodology is described in detail in Section 4.3. Application of the method to transonic and high-lift airfoil design is given in Sections 4.4 and 4.5, respectively. Section 4.6 summarizes the chapter.

4.2 Airfoil Shape Optimization

Out of a variety of design problems in aerodynamics, we focus here on airfoil shape optimization (ASO). Material concerning general aerodynamic optimization, CFD analysis, shape parameterization, and other relevant issues can be found in [26], Chapter 9.

An airfoil is a streamlined aerodynamic surface such as the one shown in Fig. 4.1. The function of the airfoil is to generate a lift force $\boldsymbol{l}$ at a range of operating conditions (Mach number M_∞, Reynolds number Re, angle of attack α). The drag force increases quadratically with increasing lift. Normally, the drag force is to be minimized for a given lift. These forces are non-dimensionalized by divinding them by $q_\infty S$, where $q_\infty \equiv (1/2)\rho_\infty V_\infty^2$ is the dynamic pressure, ρ_∞ is the air density, V_∞ is the free-stream velocity, and S is a reference surface. After non-dimensionalization they are called the lift coefficient, denoted by C_l, and the drag coefficient, denoted by C_d.

In direct ASO, the objective is to determine an airfoil shape that maximizes a performance criterion for a given set of constraints at a particular operating condition. Usually, the lift coefficient is maximized, the drag coefficient is minimized, or the lift-to-drag ratio is maximized. For example, if the lift coefficient is maximized, then a constraint is necessary on the maximum allowable drag coefficient. Further constraints are often included, e.g., to account for the wing structural components inside the airfoil one sets a constraint on the airfoil cross-sectional area. In inverse ASO, the airfoil shape is designed to attain a specific flow behavior which is defined a priori. Typically, a target airfoil surface pressure distribution is prescribed.

The optimization methodology described in this chapter is illustrated using the direct ASO approach. However, the method itself is more general and can also be applied to inverse airfoil design.

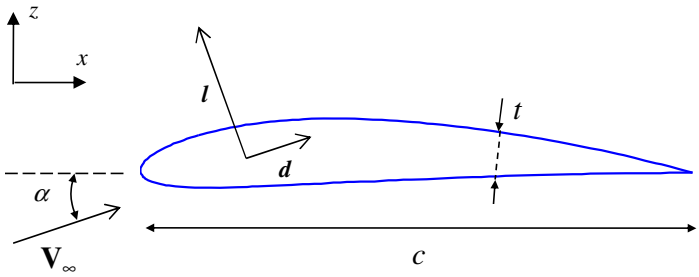

Fig. 4.1 A single-element airfoil section of chord length c and thickness t. $\mathbf{V}_\infty$ is the free-stream velocity at an angle of attack α relative to the x-axis. $\boldsymbol{l}$ is the lift force (perpendicular to $\mathbf{V}_\infty$) and $\boldsymbol{d}$ is the drag force (parallel to $\mathbf{V}_\infty$).

4.3 Optimization Methodology

In this section, we formulate the variable-fidelity airfoil optimization methodology that exploits the CFD-based low-fidelity models and the shape-preserving response prediction [18] methodology as the model correction tool. The NACA four-digit airfoil parameterization method is used due to its simplicity. The details of this parameterization, as well as the details of the CFD modeling methodology using the grid generator ICEM CFD [19] and the flow solver FLUENT [20] can be found in [26], Chapter 9.

4.3.1 General Description

The method follows the general principles of SBO [7, 8], as shown in Fig. 4.2, where the optimization burden is shifted to the low-cost surrogate model (referred to as *s*), whereas the high-fidelity model (referred to as *f*) is referenced occasionally for verification purposes and to obtain data necessary to update the surrogate. The surrogate is a corrected physics-based low-fidelity model (referred to as *c*).

The low-fidelity model is corrected to become a reliable representation of the high-fidelity model. Normally, the figures of interest in the optimization, i.e., the objectives and constraints, are aligned between the high-fidelity and low-fidelity models using a correction procedure, e.g., space mapping [14]. However, in the

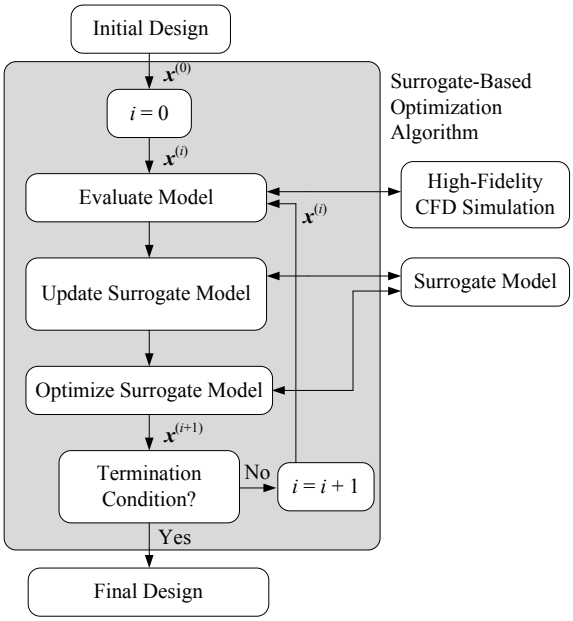

Fig. 4.2 A flowchart of the surrogate-based optimization algorithm

case of aerodynamic shape optimization, the figures of interest, such as the lift and drag coefficients, are scalars for a given operating condition and a given design vector **x**, which results in non-uniqueness of any alignment procedure that could be applied in order to match the low-fidelity model with the high-fidelity one, unless a sufficiently large amount of high-fidelity data is used in the model matching process.

Here, the model alignment is performed using intermediate simulation results, more specifically, the pressure and skin friction distributions, whose dimensionality can be made as large as necessary by selecting sufficient number of control points along the airfoil chord. As the objectives and constraints are uniquely determined by the pressure and skin friction distributions, alignment of the corresponding distributions for the low- and high-fidelity models will result in an (unique) alignment of the figures of interest. The SPRP methodology [18] is adopted here for the alignment procedure.

4.3.2 Surrogate Modeling Using Shape-Preserving Response Prediction

The SPRP model is formulated here using the pressure distribution. The formulation for the skin friction part is analogous. We denote the pressure distributions for the high- and low-fidelity models as $C_{p.f}$ and $C_{p.c}$, respectively. The surrogate model is constructed assuming that the change of $C_{p.f}$ due to the adjustment of the design variables **x** can be predicted using the actual changes of $C_{p.c}$. The change of $C_{p.c}$ is described by the translation vectors corresponding to certain (finite) number of its characteristic points on the pressure distribution. These translation vectors are subsequently used to predict the change of $C_{p.f}$, whereas the actual $C_{p.f}$ at the current design, $C_{p.f}(\mathbf{x}^{(i)})$, is treated as a reference.

Figure 4.3(a) shows the pressure distribution $C_{p.c}$ of the low-fidelity model at $\mathbf{x}^{(i)} = [0.02\ 0.4\ 0.12]^T$ (NACA 2412 airfoil) for $M_\infty = 0.7$ and $\alpha = 1$ deg, as well as $C_{p.c}$ at $\mathbf{x} = [0.025\ 0.56\ 0.122]^T$; $\mathbf{x}^{(i)}$ will denote a current design (at the ith iteration of the optimization algorithm; the initial design will be denoted as $\mathbf{x}^{(0)}$ accordingly). Circles denote characteristic points of $C_{p.c}(\mathbf{x}^{(i)})$, here, representing, among others, x/c equal to 0 and 1 (leading and trailing airfoil edges, respectively), the maxima of $C_{p.c}$ for the lower and upper airfoil surfaces, as well as the local minimum of $C_{p.c}$ for the upper surface. The last two points are useful to locate the pressure shock. Squares denote corresponding characteristic points for $C_{p.c}(\mathbf{x})$, while small line segments represent the translation vectors that determine the "shift" of the characteristic points of $C_{p.c}$ when changing the design variables from $\mathbf{x}^{(i)}$ to **x**.

In order to obtain a reliable prediction, the number of characteristic points has to be larger than illustrated in Fig. 4.3(a). Additional points are inserted in between initial points either uniformly with respect to x/c (for those parts of the pressure distribution that are almost flat) or based on the relative pressure value with respect to corresponding initial points (for those parts of the pressure distribution that are "steep"). Figure 4.3(b) shows the full set of characteristic points (initial points are distinguished using larger markers).

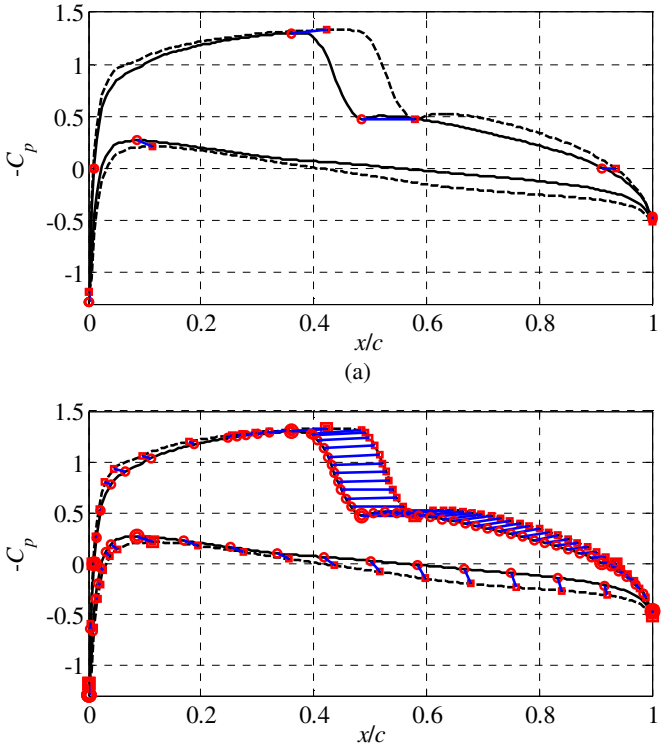

Fig. 4.3 (a) Example low-fidelity model pressure distribution at the design $\mathbf{x}^{(i)}$, $C_{p.c}(\mathbf{x}^{(i)})$ (solid line), the low-fidelity model pressure distribution at other design $\mathbf{x}$, $C_{p.c}(\mathbf{x})$ (dotted line), characteristic points of $C_{p.c}(\mathbf{x}^{(i)})$ (circles) and $C_{p.c}(\mathbf{x})$ (squares), and the translation vectors (short lines); (b) low-fidelity model pressure distributions, initial characteristic points (large markers) and translation vectors from Fig. 4.3(a) as well as additional points (small markers) inserted in between the initial points either uniformly with respect to x/c (for the "flat" parts of the pressure distribution) or based on the relative pressure value with respect to corresponding initial points (for the "steep" parts of the pressure distribution)

The pressure distribution of the high-fidelity model at the given design, here, $\mathbf{x}$, can be predicted using the translation vectors applied to the corresponding characteristic points of the pressure distribution of the high-fidelity model at $\mathbf{x}^{(i)}$, $C_{p.f}(\mathbf{x}^{(i)})$. This is illustrated in Fig. 4.4(a) where only initial characteristic points and translation vectors are shown for clarity. Figure 4.4(b) shows the predicted pressure distribution of the high-fidelity model at $\mathbf{x}$ as well as the actual $C_{p.f}(\mathbf{x})$. The agreement between both curves is very good.

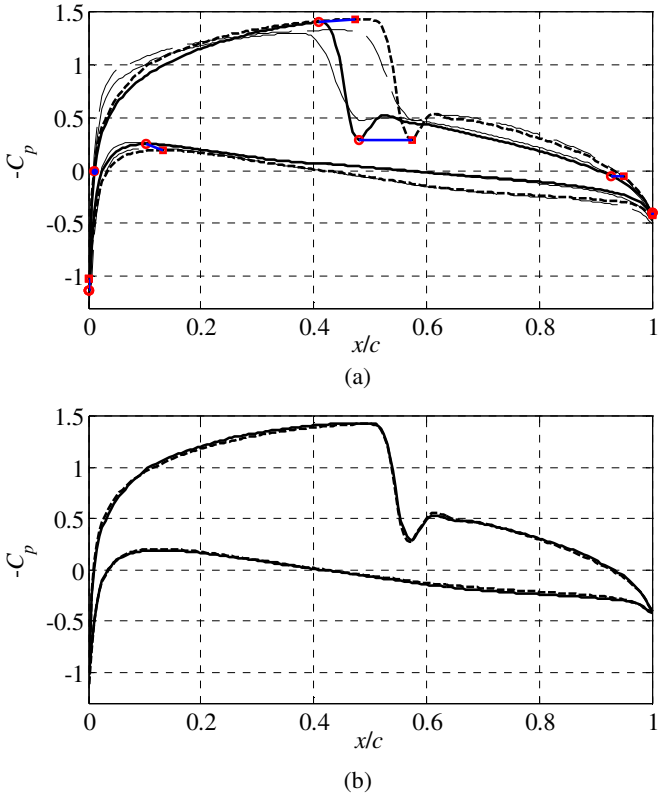

Fig. 4.4 (a) High-fidelity model pressure distribution at $\mathbf{x}^{(i)}$, $C_{p.f}(\mathbf{x}^{(i)})$ (solid line) and the predicted high-fidelity model C_p at $\mathbf{x}$ (dotted line) obtained using SPRP based on characteristic points of Fig. 4.3(b); characteristic points of $C_{p.f}(\mathbf{x}^{(i)})$ (circles) and the translation vectors (short lines) were used to find the characteristic points (squares) of the predicted high-fidelity model pressure distribution (only initial points are shown for clarity); low-fidelity model distributions $C_{p.c}(\mathbf{x}^{(i)})$ and $C_{p.c}(\mathbf{x})$ are plotted using thin solid and dotted line, respectively; (b) high-fidelity model pressure distribution at $\mathbf{x}$, $C_{p.f}(\mathbf{x})$ (solid line), and the predicted high-fidelity model pressure distribution at $\mathbf{x}$ obtained using SPRP (dotted line)

SPRP can be rigorously formulated as follows. Let $C_{p.f}(\mathbf{x}) = [c_{p.f}(\mathbf{x},y_1) \ldots c_{p.f}(\mathbf{x},y_m)]^T$ and $C_{p.c}(\mathbf{x}) = [c_{p.c}(\mathbf{x},y_1) \ldots c_{p.c}(\mathbf{x},y_m)]^T$, where y_j, $j = 1, \ldots, m$, are control points on the x/c axis (we assume that $y_{j+1} > y_j$ and $0 \le y_j \le 1$ for all j). To simplify the notation we assume that $C_{p.f}$ ($C_{p.c}$) is the pressure distribution for the upper surface only. Formulation for the lower surface is identical. Let $p_j^f = [y_j^f \;\; r_j^f]^T$, $p_j^{c0} = [y_j^{c0} \;\; r_j^{c0}]^T$, and $p_j^c = [y_{jc} \;\; r_j^c]^T$, $j = 1, \ldots, K$, denote the sets of characteristic points of $C_{p.f}(\mathbf{x}^{(i)})$, $C_{p.c}(\mathbf{x}^{(i)})$ and $C_{p.f}(\mathbf{x})$, respectively. Here, y and r denote the x/c and magnitude components of the respective point. The translation vectors of the low-fidelity model pressure distribution are defined as $T_i = [y_j^t \;\; r_j^t]^T$, $j = 1,\ldots, K$, where $y_j^t = y_j^c - y_j^{c0}$ and $r_j^t = r_j^c - r_j^{c0}$.

The SPRP surrogate model is defined as follows

$$C_{p.s}^{(i)} = \left[c_{p.s}^{(i)}(\mathbf{x}, y_1) \ldots c_{p.s}^{(i)}(\mathbf{x}, y_m)\right]^T \tag{4.1}$$

where

$$c_{p.s}^{(i)}(\mathbf{x}, y_j) = \bar{c}_{p.f}(\mathbf{x}^{(i)}, F(y_j, \{-y_k^t\}_{k=1}^K)) + r(y_j, \{r_k^t\}_{k=1}^K) \tag{4.2}$$

for $j = 1, \ldots, m$. $\bar{c}_{p.f}(\mathbf{x}, y)$ is an interpolation of $\{c_{p.f}(\mathbf{x},y_1), \ldots, c_{p.f}(\mathbf{x},y_m)\}$ onto the interval [0,1]. The scaling function F interpolates the data pairs $\{y_1,y_1\}$, $\{y_1^f,y_1^f-y_1^t\}$, …, $\{y_K^f,y_K^f-y_K^t\}$, $\{y_m,y_m\}$, onto the interval [0,1]. The function r does a similar interpolation for data pairs $\{y_1,r_1\}$, $\{y_1^f,r_1^f-r_1^t\}$, …, $\{y_K^f,r_K^f-r_K^t\}$, $\{y_m,r_m\}$; here $r_1 = c_{p.c}(\mathbf{x},y_1) - c_{p.c}(\mathbf{x}^r,y_1)$ and $r_m = c_{p.c}(\mathbf{x},y_m) - c_{p.c}(\mathbf{x}^r,y_m)$. Note that $C_{p.s}^{(i)}(\mathbf{x}^{(i)}) = C_{p.f}^{(i)}(\mathbf{x}^{(i)})$ as all translation vectors are zero at $\mathbf{x} = \mathbf{x}^{(i)}$.

The prediction method assumes that the high- and low-fidelity model pressure distributions have corresponding sets of characteristic points. This is usually the case for the practical ranges of design variables because the overall shape of the distributions is similar for both models. In case of a lack of correspondence, original definitions of characteristic points are replaced by their closest counterparts. The typical example would be non-existence of the local minimum of the pressure distribution for the upper surface for the high- and/or low-fidelity model at certain designs. In this case, the original point (local minimum) is replaced by the points characterized by the largest curvature.

4.3.3 Objective Function

Due to unavoidable misalignment between the pressure distributions of the high-fidelity model and its SPRP surrogate at the designs other than the one at which the model is determined, i.e., $\mathbf{x}^{(i)}$, it is not convenient to handle constraints (e.g., drag) directly, because the design that is feasible for the surrogate model, may not be feasible for the high-fidelity model. In particular, the design obtained as a result of optimizing the surrogate model $C_{p.s}^{(i)}$, i.e., $\mathbf{x}^{(i+1)}$, will be feasible for $C_{p.s}^{(i)}$. However, if $\mathbf{x}^{(i+1)}$ is not feasible for the high-fidelity model, it will not be feasible for $C_{p.s}^{(i+1)}$ because we have $C_{p.s}^{(i+1)}(\mathbf{x}^{(i+1)}) = C_{p.f}(\mathbf{x}^{(i+1)})$ by the definition of the surrogate model. In order to alleviate this problem, we shall use the penalty function approach to handle the constraints.

More specifically, if the figure of interest is the lift coefficient, while the drag and the airfoil cross-sectional area are constraints, the objective function is defined as

$$H(C_p(\mathbf{x})) = -C_{l.s}(C_p(\mathbf{x})) + \beta\left[\Delta C_{d.s}(C_p(\mathbf{x}))\right]^2 + \gamma\left[\Delta A(\mathbf{x})\right]^2 \tag{4.3}$$

where $\Delta C_{d.s} = 0$ if $C_{d.s} \le C_{d.s.max}$ and $\Delta C_{d.s} = C_{d.s} - C_{d.s.max}$ otherwise, and $\Delta A = 0$ if $A \ge A_{min}$ and $\Delta A = A - A_{min}$ otherwise. In the numerical experiments, presented in the next section, we use $\beta = \gamma = 1000$. Here the pressure distribution for the

surrogate model is $C_p = C_{p.s}$, and for the high-fidelity model $C_p = C_{p.f}$. Also, $C_{l.s}$ and $C_{d.s}$ denote the lift and drag coefficients (both being functions of the pressure distribution).

4.3.4 Optimization with SPRP Surrogate

The efficiency of variable-fidelity optimization with SPRP model is illustrated by airfoil design at $M_\infty = 0.75$ and $\alpha = 0°$. The initial design is set as NACA 2412 and the objective function is defined by Eq. (4.3), with $C_{d.s.max} = 0.0040$ and $A_{min} = 0.075$. The side constraints on the design variables are $0 \le m \le 0.03$, $0.3 \le p \le 0.6$, and $0.09 \le t \le 0.13$. Constraint tolerance bands are set to 5%.

The high-fidelity model is based on the Euler equations and it is solved as described in [26], Chapter 9. The low-fidelity model is the transonic small-disturbance equation (TSDE) and it is solved using the computer code TSFOIL [21], which was developed at NASA in the 1970s. The code is capable of solving the TSDE for flow past lifting airfoils in both free air and various wind-tunnel environments by using a finite-difference method and an iterative successive line over-relaxation (SLOR) algorithm. The computational grid is a simple, fixed Cartesian grid.

Five iterations of the SPRP-based design methodology were executed. The computational cost is 5 high-fidelity and 161 surrogate model evaluations. The surrogate model optimization is performed using the pattern-search algorithm [22]. The results are given in Table 4.1. As the surrogate model evaluates quite fast (about 1 to 3 seconds depending on the design) and the high-fidelity model evaluation takes a few minutes, the total cost of evaluating the low-fidelity model in the whole optimization run corresponds to roughly 1-2 evaluations of the high-fidelity model. The equivalent number of high-fidelity model evaluations is less than 7 for this particular case.

Table 4.1 Numerical results of the design optimization. All the numerical values are from the high-fidelity model. N_c is number of low-fidelity model evaluations and N_f is the number high-fidelity model evaluations.

Variable	Initial	Direct[#]	VF-SPRP[$]
m	0.0200	0.0160	0.0173
p	0.4000	0.5999	0.5930
t	0.1200	0.1199	0.1163
C_l	0.4732	0.4770	0.5085
C_d	0.0100	0.0040	0.0041
A	0.0808	0.0808	0.0783
N_c	N/A	0	161
N_f	N/A	130	5
Total cost[*]	N/A	130	< 7

[#] Direct optimization of the high-fidelity model using the pattern-search algorithm [22].
[$] Design obtained using the methodology described here and the pattern-search algorithm [22].
[*] The total optimization cost is expressed in the equivalent number of high-fidelity model evaluations.

The optimizer achives this design by reducing maximum ordinate of the mean camber line (m) from 2% to 1.6%, and moving the location of the maximum camber (p) is rearward from 40% to 59% (which is close to the side constraint upper limit).

By reducing the camber, the flow velocity decreases on the upper surface and the shock strength is reduced. This can be seen in Fig. 4.5. By moving the maximum camber rearward, the aft camber increases and the pressure distribution opens up behind the shock, where flow is subsonic, and lift is increased by 3.5 lift counts (one lift count is $\Delta C_l = 0.01$). This can be seen in Fig. 4.6. The drag is reduced to satisfy the constraint limit. This is achived by reducing the thickness from 12% to 11.6%.

The case was also performed by direct optimization of the high-fidelity model using the pattern-search algortihm. Direct optimization obtained a very simlar optimal design, but required 130 high-fidelity model evaluations.

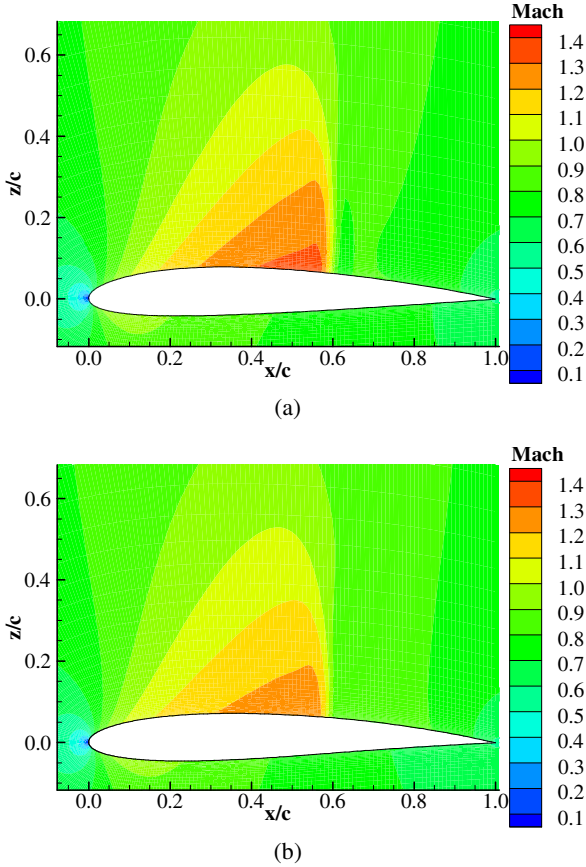

Fig. 4.5 (a) Mach number contours for the initial design (NACA 2412) at $M_\infty = 0.75$ and $\alpha = 0°$, (b) Mach number contours of the optimum design at the operating condition as in (a)

It should be emphasized that despite the encouraging results obtained for the considered test case, the use of the TSFOIL code may be problematic in general. In particular, TSFOIL would not converge to a valid flow solution for all designs in the solution domain. This may results in the convergence problems of the optimization algorithm. Furthermore, it turns out that the TSDE-based surrogate does not give a sufficiently reliable prediction of the drag coefficient. In particular, for small (local) changes of the design variables the low-fidelity model does not follow closely of the high-fidelity model.

The conclusions drawn from this study are:

- a proper low-fidelity model needs to be selected to provide a reliable prediction of the high-fidelity model, especially for small changes in the design variables,
- the low-fidelity model has to be reliable in terms of execution, and
- the optimization algorithm should be endowed with suitable convergence safeguards.

4.3.5 Optimization Algorithm

In this section, we formulate the optimization algorithm exploiting the SPRP-based surrogate model and a trust-region convergence safeguard [23]. This algorithm is used to solve the transonic and high-lift airfoil design cases, presented in Sections 4.4 and 4.5. The algorithm flow can be summarized as follows:

1. Set $i = 0$; Select λ (initial trust region radius); Evaluate $C_{p.f}(\mathbf{x}^{(0)})$;
2. Setup SPRP model;
3. Obtain $\mathbf{x}^{(i+1)} = \text{argmin}\{l \leq \mathbf{x} \leq u, \|\mathbf{x} - \mathbf{x}^{(i)}\| \leq \lambda : H(C_{p.s}{}^{(i)}(\mathbf{x}))\}$;
4. Evaluate high-fidelity model to get $C_{p.f}(\mathbf{x}^{(i)})$;
5. If $H(C_{p.f}{}^{(i)}(\mathbf{x}^{(i+1)})) < H(C_{p.f}{}^{(i)}(\mathbf{x}^{(i)}))$ accept $\mathbf{x}^{(i+1)}$; Otherwise $\mathbf{x}^{(i+1)} = \mathbf{x}^{(i)}$;
6. Update λ;
7. Set $i = i + 1$;
8. If termination condition is not satisfied, go to 2.

The SPRP surrogate model is updated before each iteration of the optimization algorithm using the high-fidelity model data at the design obtained in the previous iteration. The trust-region parameter λ is updated after each iteration, i.e., decreased if the new design was rejected or the improvement of the high-fidelity model objective function was too small compared to the prediction given by the SPRP surrogate, or increased otherwise. Classical updating rules are used (see, e.g., [23, 24]). The algorithm is terminated if $\|\mathbf{x}^{(i+1)} - \mathbf{x}^{(i)}\| < 0.001$ or $\lambda < 0.001$.

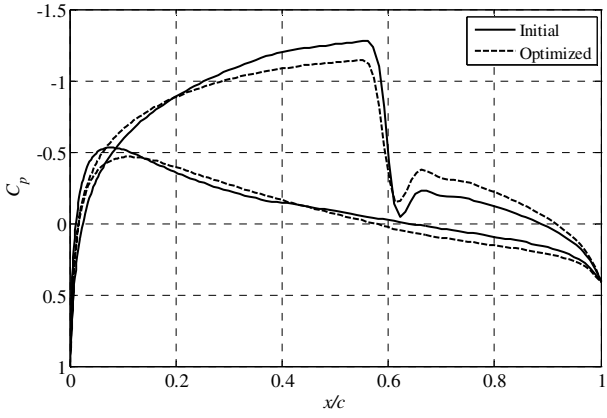

(a)

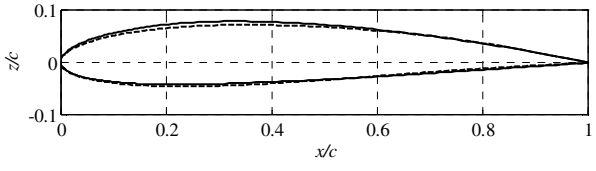

(b)

Fig. 4.6 (a) Pressure distributions of the initial (solid) and optimized (dashed) airfoil shapes, (b) initial (solid) and optimized (dashed) airfoil shapes

4.4 Transonic Airfoil Design

In this section, the variable-fidelity optimization algorithm is applied to airfoil design at a steady transonic flow condition. The surrogate model optimization is performed using the pattern-search algorithm [22]. The results of the design methodology are compared to the results obtained through direct optimization of the high-fidelity model.

4.4.1 Case Setup

The initial design is set as NACA 3210 and the the objective function is defined by Eq. (4.3), with $C_{d.s.max}$ =0.0041 and A_{min} = 0.065. The operating condition is M_∞ = 0.75 and α = 1°. The side constraints on the design variables are $0 \leq m \leq 0.1$, $0.2 \leq p \leq 0.8$, and $0.05 \leq t \leq 0.20$. Constraint tolerance bands are set to 5%.

4.4.2 Model Setup

In this case, variable-resolution modeling is employed. The high- and low-fidelity models solve the Euler equations, but the low-fidelity model uses a coarser

computational mesh and relaxed convergence criteria. The particulars of the low-fidelity model mesh and convergence criteria are found by performing a parametric study on a typical airfoil section.

The NACA 2412 was selected for the parametric study. The Mach number is taken to be $M_\infty = 0.75$ and the angle of attack is set to $\alpha = 1$ deg. First a fine mesh is developed with a total of 320 points in the y-direction, 180 points on the airfoil surface and 160 points in the wake behind the airfoil, with a total of 106 thousand cells. Then, the flow is solved to full convergence to get the reference values. The convergence history is shown in Fig. 4.7(a). The solver needed 216 iterations to reach a converged solution based on the residuals. However, the lift and drag

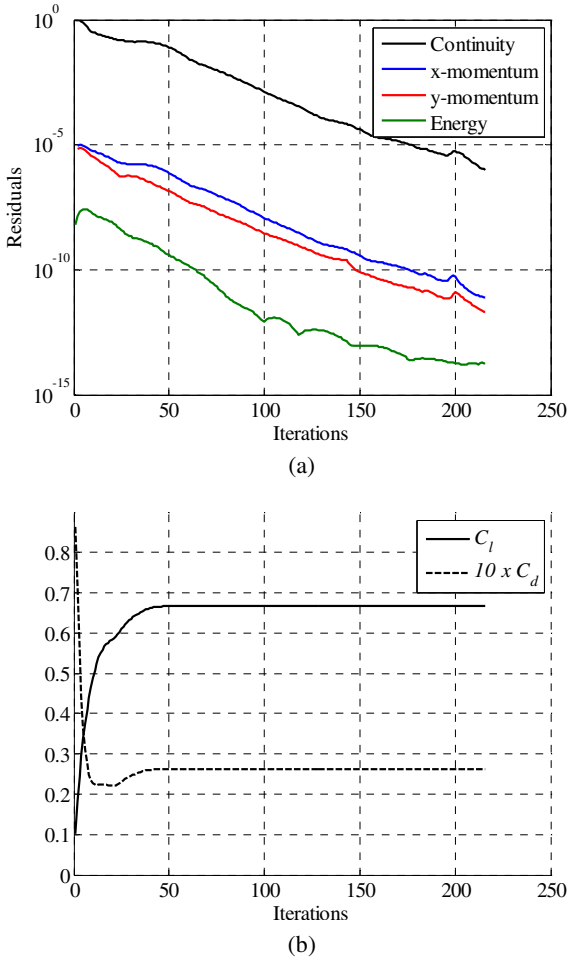

Fig. 4.7 (a) Convergence history of the simulation of the flow past the NACA 2412 at $M_\infty = 0.75$ and $\alpha = 1$ deg., (b) convergence of the lift and drag coefficients. The converged values of the lift coefficient is $C_l = 0.67$ and the drag coefficient is $C_d = 0.0261$.

coefficient values have reached a converged value after approximately 50 iterations, as can be seen in Fig. 4.7(b). Therefore, the number of iterations limit is set to 100 iterations in the subsequent steps.

Subsequently, the number of mesh points was reduced. This was done in two steps. First, the number of mesh points in the y-direction and the number of mesh points behind the airfoil were halved in each step. Then, the number of mesh points on the airfoil surface was reduced incrementally. In each step, the pressure distribution was plotted. This was done so the overall number mesh points could be reduced as much as possible, without reducing the mesh density on the airfoil surface, so that the shock could be resolved adequately.

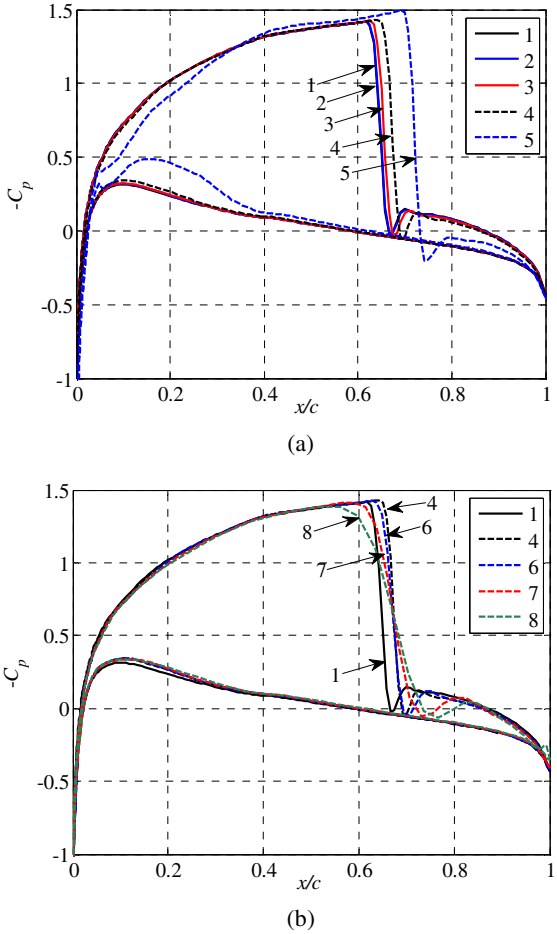

Fig. 4.8 (a) Pressure distributions for the first part of the parametric mesh study where the mesh points are reduced in the y-direction and in the wake behind the airfoil, (b) pressure distributions for the second part where the mesh points are reduced on the airfoil surface. The Mach number is $M_\infty = 0.75$ and the angle of attack is $\alpha = 1$ deg.

The results of the first mesh reduction are shown in Fig. 4.8(a). In the first four steps the number of cells is reduced from 106 thousand to 8295, but the pressure distribution does not change significantly, aside in the region of the shock, where the shock has strengthened and moved aft by less than 2.5% of the chord length.

This has led, however, to a significant increase in the estimation of the drag coefficient (+23.7%), as can be seen in Fig. 4.9(a), and a moderate increase in the lift coefficient (+2.7%). The evaluation time has been reduced from 470 s to 40 s (Fig. 4.9(b)). In the last step the number of mesh points in the y-direction is reduced to only 12 and the total number of cells is 3750. Now, there is a large change in the shock strength and location, but the pressure distribution is also

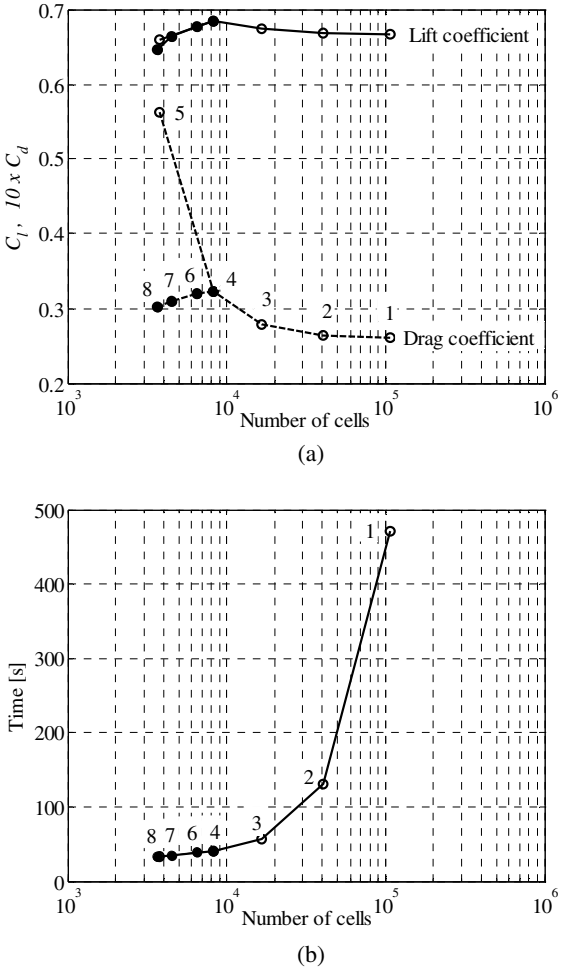

Fig. 4.9 (a) Lift and drag coefficients as a function of the number of cells for the parametric mesh study, (b) evaluation time of the CFD simulation model as a function of the number of cells. The Mach number is $M_\infty = 0.75$ and the angle of attack is $\alpha = 1$ deg.

altered in the front part the airfoil, leading to a large increase in the drag coefficient and a reduction in the lift coefficient.

The fourth mesh was selected for the second mesh reduction. The results are shown in Fig. 4.8(b). The number of mesh points on the airfoil surface was reduced by 50 in the first two steps (meshes 6 and 7) and then by 20 (mesh 8). It is clear, as the mesh gets coarser on the airfoil surface, the shock is smeared over a larger area and the estimated shock strength is reduced. As can be seen from Fig. 4.9 (a), both the drag and lift coefficients are reduced in this process. The overall evaluation time is reduced to about 34 s in the last step (Fig. 4.9(b)).

The second but last mesh (number 7) was selected as a basis to construct the low-fidelity model. The mesh has 48 points in the y-direction, 115 points on the airfoil surface, and 20 points in the wake behind the airfoil, with a total of 8295 thousand cells. The reason for selecting this particular mesh is that the difference in evaluation time is insignificant between the last two meshes (7 and 8), but the difference in the shock is quite substantial: it is easier to correct the low-fidelity model if the difference between it and the high-fidelity model is smaller.

For the airfoil considered in this parametric study, the overall evaluation time for the low-fidelity model using the above mentioned mesh, and an iteration limit of 100, is about 35 s, which is approximately 13.5 times faster than the high-fidelity model using the fine mesh and traditional convergence criteria. The criteria used in this work for the high-fidelity model is a maximum residual of 10^{-6}, or a maximum number of iterations of 1000. The overall evaluation time of the high-fidelity model in this parametric study is 471 s with a total of 216 iterations. In many cases the solver does not fully converge with respect to the residuals and goes on up to 1000 iterations. Then the overall evaluation time goes up to 2500 s, and the low-fidelity model is approximately 73 times faster. Note that the evaluation times reported here includes the time required for connecting to twice to the license server, once for the grid generator, ICEM CFD [19], and once for the flow solver, FLUENT [20].

4.4.3 Results and Discussion

The optimization method presented here was able to meet the design goals and yield the optimized design—within the given constraint bands—using 330 low-fidelity model evaluations and 11 high-fidelity model evaluations (Table 4.2). The equivalent number of high-fidelity model evaluations is less than 18 (using the ratio of the high-fidelity model evaluation time to the corrected low-fidelity model as 50). The direct method obtained a similar optimized design, but required 120 high-fidelity model evaluations.

To meet the design goals, the optimizer does three fundamental shape changes: (i) the maximum ordinate of the mean camber line (m) is reduced or kept constant, (ii) the location of the maximum ordinate of the mean camber line (p) is moved aft, thus increasing the trailing-edge camber, and (iii) the thickness (t) is reduced. Shape changes (i) and (iii) reduce the shock strength and, thus, reduce the drag coefficient. The associated change in the pressure distribution reduces the lift coefficient. However, shape change (ii) improves (or recovers a part of) the lift by opening up the pressure distribution behind the shock. These effects are clearly

demonstrated in the pressure distribution plot in Fig. 4.10(a), the airfoil shape plots in Fig. 4.10(b), and the Mach contour plots in Figs. 4.11(a) and 4.11(b).

Table 4.2 Numerical results for lift maximization while keeping drag below a desired value at $M_\infty = 0.75$ and $\alpha = 1$ deg. All the numerical values are from the high-fidelity model. N_c and N_f are the numbers of low- and high-fidelity model evaluations, respectively

Variable	Initial	Direct[#]	VF-SPRP[$]
m	0.0300	0.0080	0.0090
p	0.2000	0.6859	0.6732
t	0.1000	0.1044	0.1010
C_l	0.8035	0.4641	0.4872
C_d	0.0410	0.0041	0.0040
A	0.0675	0.0703	0.0680
N_c	N/A	0	330
N_f	N/A	120	11
Total cost[*]	N/A	120	< 18

[#] Direct optimization of the high-fidelity model using the pattern-search algorithm [22].
[$] Design obtained using the algorithm described in Section 4.3; surrogate model optimization performed using the pattern-search algorithm [22].
[*] The total optimization cost is expressed in terms of the equivalent number of high-fidelity model evaluations. The ratio of the high-fidelity model evaluation time to the corrected low-fidelity model evaluation time varies between 13.5 to 73 depending on the design. We use a fixed value of 50 here.

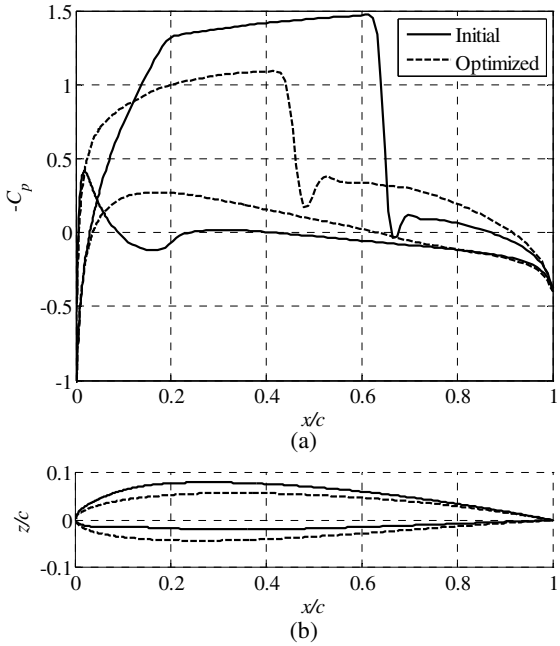

Fig. 4.10 (a) Pressure distribution of initial (solid) and optimized (dashed) airfoils, (b) initial (solid) and optimized (dashed) airfoil shapes. The Mach number is $M_\infty = 0.75$ and the angle of attack is $\alpha = 1$ deg.

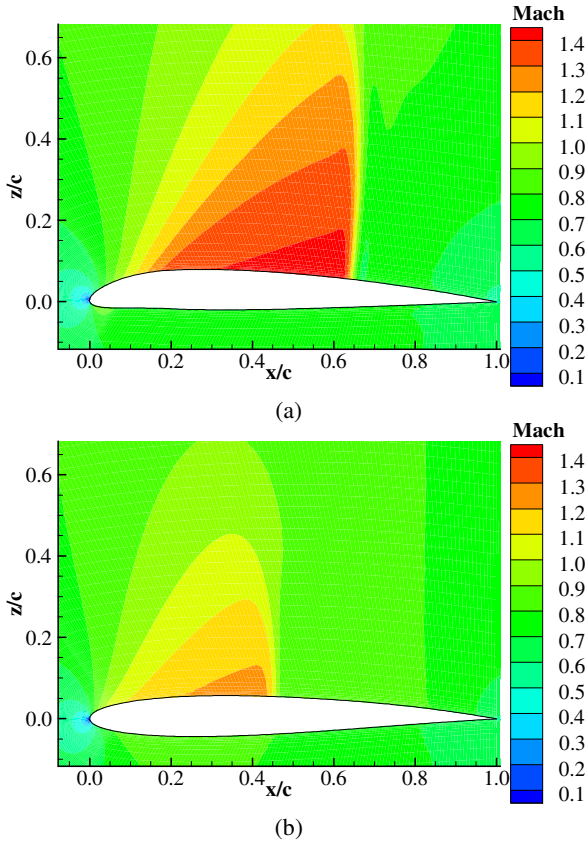

Fig. 4.11 Mach contour plots of (a) the initial airfoil, (b) the optimized airfoil. The Mach number is $M_\infty = 0.75$ and the angle of attack is $\alpha = 1$ deg.

The variable-resolution modeling exploited in this study exhibits consistent behavior, i.e., the changes of the pressure distribution (and, consequently, the figures of interest such as lift and drag) of the low-fidelity model closely follows that of the high-fidelity one. This was not the case in the example in Section 4.3.4, where variable-fidelity physics modeling was exploited with the Euler equations and TSDE.

4.5 High-Lift Airfoil Design

In this section, design optimization of a single-element airfoil at steady subsonic high-lift condition is considered. As before, the surrogate model optimization is performed using the pattern-search algorithm [22] and the results of the design methodology are compared to the results obtained through direct optimization of the high-fidelity model.

4.5.1 Case Setup

The Mach number is set to $M_\infty = 0.2$, the angle of attack is $\alpha = 12$ degree, and the Reynolds number is $Re = 2.3$ million. The initial design is set as NACA 0012 and the the objective function is defined by Eq. (3), but with the skin friction distribution C_f included, as viscous effects are important at this condition. The maximum allowable drag is set to $C_{d.s.max} = 0.0212$. The area constraint is not used here. The side constraints on the design variables are $0 \le m \le 0.08$, $0.3 \le p \le 0.6$, and $0.08 \le t \le 0.14$. Constraint tolerance bands are set to 5%.

4.5.2 Model Setup

The high-fidelity model f solves the RANS equations with the Spalart-Allmaras one equation turbulence model [25]. The details of the CFD model are as described in [26], Chapter 9. The low-fidelity model c is constructed as a low-order polynomial approximation of the high-fidelity model data, i.e., both the pressure distribution $C_{p.f}$ and the skin friction distribution $C_{f.f}$. The low-fidelity model is established in the entire design using evaluations of f at the following seven designs: $\mathbf{x}^0 = [0.04\ 0.45\ 0.11]^T$ (center point), and $\mathbf{x}^1 = [0.0\ 0.45\ 0.11]^T$, $\mathbf{x}^2 = [0.08\ 0.45\ 0.11]^T$, $\mathbf{x}^3 = [0.04\ 0.3\ 0.11]^T$, $\mathbf{x}^4 = [0.04\ 0.6\ 0.11]^T$, $\mathbf{x}^5 = [0.04\ 0.45\ 0.08]^T$, $\mathbf{x}^6 = [0.044\ 0.45\ 0.14]^T$ (single-variable perturbations for all design variables). The low-fidelity model is defined as a reduced quadratic model (no mixed terms)

$$c(\mathbf{x}) = \lambda_0 + \lambda_1 m + \lambda_2 p + \lambda_3 t + \lambda_4 m^2 + \lambda_5 p^2 + \lambda_6 t^2 \tag{4.4}$$

where the coefficients λ are found by solving the linear system $c(\mathbf{x}^j) = f(\mathbf{x}^j)$, $j = 0, 1, \ldots, 6$.

The reason for choosing the approximation-based model c is that the pressure distribution does not change significantly for the design space considered in this case. The simple model (4.4) is a reasonable compromise between the accuracy and the computational cost of creating the response surface. Still, the low-fidelity model has to be corrected in order to become a reliable representation of the high-fidelity one in the optimization process.

Figure 4.12 shows the construction of the SPRP model for the high-lift airfoil design. When compared to the transonic case, the pressure distribution is simpler (no pressure shock). However, the figures of interest (particularly drag) are very sensitive to the changes of the distribution, so that much attention has to be put to detailed "description" of the distribution through SPRP characteristic points, particularly for x/c close to zero, where the pressure gradients with respect to x/c are large. The pressure distributions of the low-fidelity model are illustrated in Fig. 4.12, at $\mathbf{x}^{(i)} = [0.01\ 0.40\ 0.09]^T$ for $M_\infty = 0.2$ and $\alpha = 10°$, as well as $C_{p.c}$ at $\mathbf{x} = [0.02\ 0.35\ 0.10]^T$. The pressure distribution of the high-fidelity model at the given design, here, $\boldsymbol{x}$, is predicted using the translation vectors applied to the corresponding characteristic points of the pressure distribution of the high-fidelity model at $\mathbf{x}^{(i)}$, $C_{p.f}(\boldsymbol{x}^{(i)})$. This is illustrated in Fig. 4.13. The predicted pressure distribution (magnified parts only) of the high-fidelity model at $\boldsymbol{x}$ as well as the actual $C_{p.f}(\mathbf{x})$ is shown in Fig. 4.14.

4.5.3 Results and Discussion

The optimization method of Section 4.3 with the low-fidelity model (4.4) improves the lift coefficient from 1.235 to 1.491 (+25.6 lift counts) by increasing camber by 2.34% and moving the location of maximum camber more aft, from 0.45 to 0.60, which is the upper bound (Table 4.3). The thickness is increased from 12% to 14% (which is the upper bound). A comparison of the initial and optimized airfoil shapes is given in Fig. 4.15(c). The optimized design is achieved by using only 11 high-fidelity CFD evaluations. The direct optimization method required 65 high-fidelity CFD evaluations and improves the lift only by 11.3%.

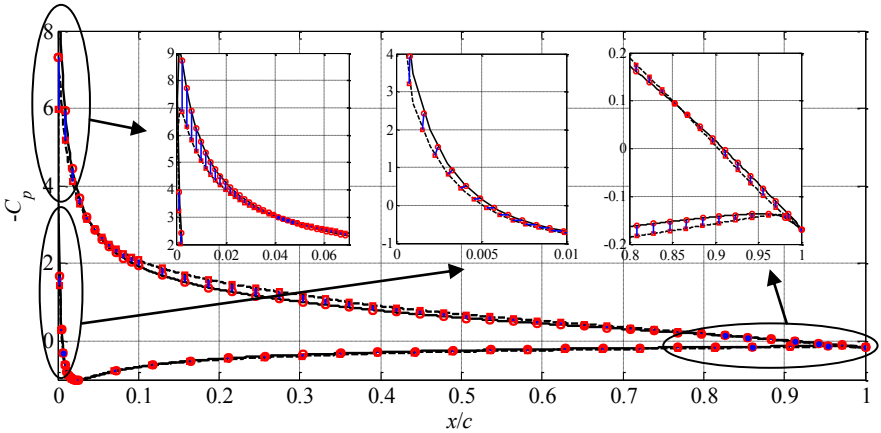

Fig. 4.12 Example low-fidelity model pressure distribution at the design $\mathbf{x}^{(i)}$, $C_{p.c}(\mathbf{x}^{(i)})$ (solid line), the low-fidelity model pressure distribution at other design $\mathbf{x}$, $C_{p.c}(\mathbf{x})$ (dotted line), characteristic points of $C_{p.c}(\mathbf{x}^{(i)})$ (circles) and $C_{p.c}(\mathbf{x})$ (squares), and the translation vectors (short lines). Only selected points and vectors are shown for the sake of clarity of the picture. Selected parts of the distributions are magnified.

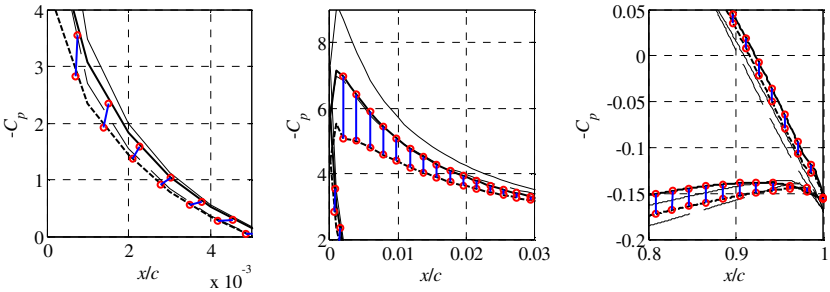

Fig. 4.13 High-fidelity model pressure distribution at $\mathbf{x}^{(i)}$, $C_{p.f}(\mathbf{x}^{(i)})$ (solid line) and the predicted high-fidelity model C_p at $\mathbf{x}$ (dotted line) obtained using SPRP based on characteristic points of Fig. 4.12; characteristic points of $C_{p.f}(\mathbf{x}^{(i)})$ (circles) and the translation vectors (short lines) were used to find the characteristic points (squares) of the predicted high-fidelity model pressure distribution

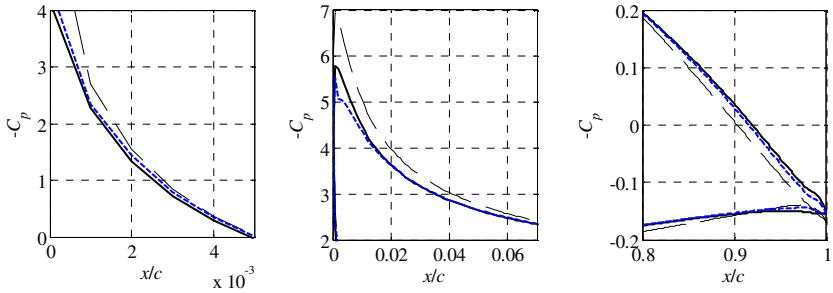

Fig. 4.14 High-fidelity model pressure distribution at **x**, $C_{p,f}(\mathbf{x})$ (solid line), and the predicted high-fidelity model pressure distribution at **x** obtained using SPRP (thick dotted line). Low-fidelity model pressure distribution at **x** is shown using a thin dashed line. SPRP model ensures better accuracy than the low-fidelity model.

Table 4.3 Numerical results for lift maximization while keeping drag below a desired value at $M_\infty = 0.2$, $\alpha = 12$ deg, and $Re = 2.3$ million

Variable	Initial	Direct[#]	VF-SPRP[$]
m	0.0000	0.0150	0.0234
p	0.4500	0.4840	0.6000
t	0.1200	0.1247	0.1400
C_l	1.235	1.392	1.491
C_d	0.0212	0.0212	0.0210
Design cost	N/A	65	11

[#] Direct optimization of the high-fidelity CFD model using the pattern-search algorithm [22].
[$] Design obtained using the algorithm described in Section 4.3; surrogate model optimization performed using the pattern-search algorithm [22].

There are three major changes in the optimized design when compared to the initial one. First of all, the increased camber opens up the pressure distribution over the whole airfoil, as can be seen in Fig. 4.15(a), and thus the lift increases.

Also, the aft camber opens the pressure distribution up near the trailing-edge, also increasing lift. Finally, the increased thickness reduces the pressure peak near the leading-edge, thus creating a milder expansion around the leading-edge, and thereby reducing pressure drag. The result is an optimized airfoil with improved lift coefficient at the same drag coefficient. A comparison of the lift and drag curves is given in Fig. 4.16. Although the airfoil was optimized at $\alpha = 12°$, the entire lift curve is shifted upwards. In this case, the angle of attack at maximum lift increases slightly (approximately by 1°).

Figure 4.17 shows the optimization history. In particular, one can observe a convergence plot (Fig. 4.17(a)), as well as the evolution of the objective function (Fig. 4.17(b)), the lift coefficient (Fig. 4.17(c)) and the drag coefficient (Fig. 4.17(d)). It follows that the algorithm exhibits a good convergence pattern and that the mechanisms introduced in the algorithm (in particular the trust region approach and the penalty function) enforce the drag limitation to be satisfied while increasing the lift coefficient as much as possible.

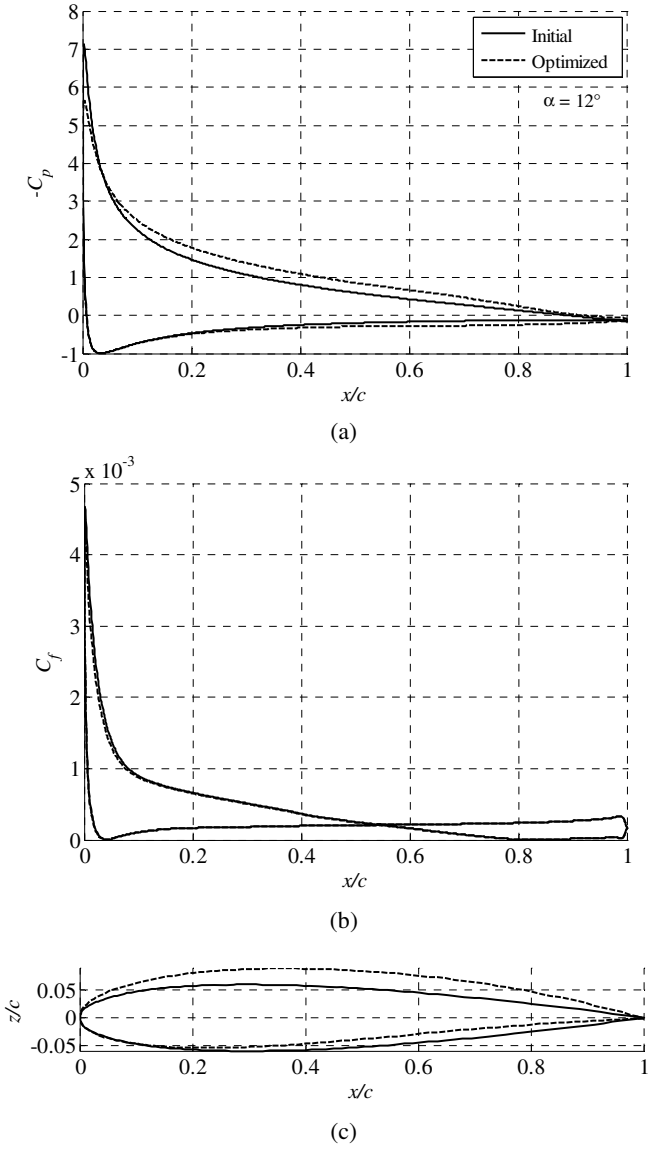

Fig. 4.15 Comparison of initial and optimized designs at $M_\infty = 0.2$, $\alpha = 12$ deg, and $Re = 2.3$ million; (a) Pressure distributions of the initial and optimized designs, (b) skin friction distributions of the initial and optimized designs, (c) initial and optimized airfoil shapes

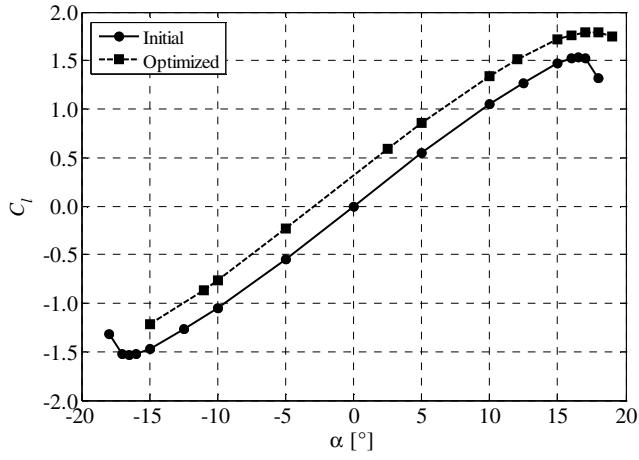

(a)

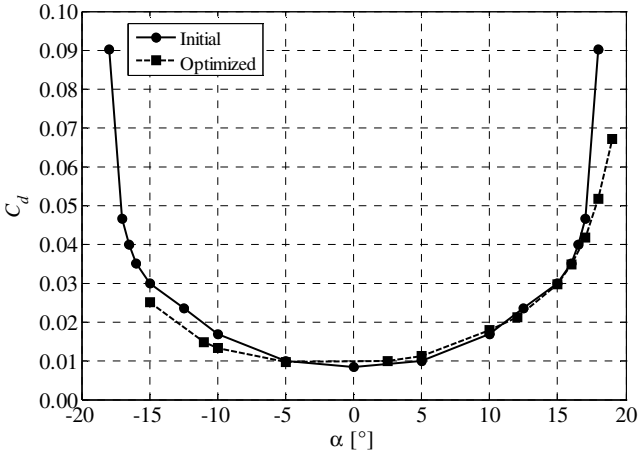

(b)

Fig. 4.16 A comparison of the lift and drag curves of the initial and optimized designs at $M_\infty = 0.2$ and $Re = 2.3$ million

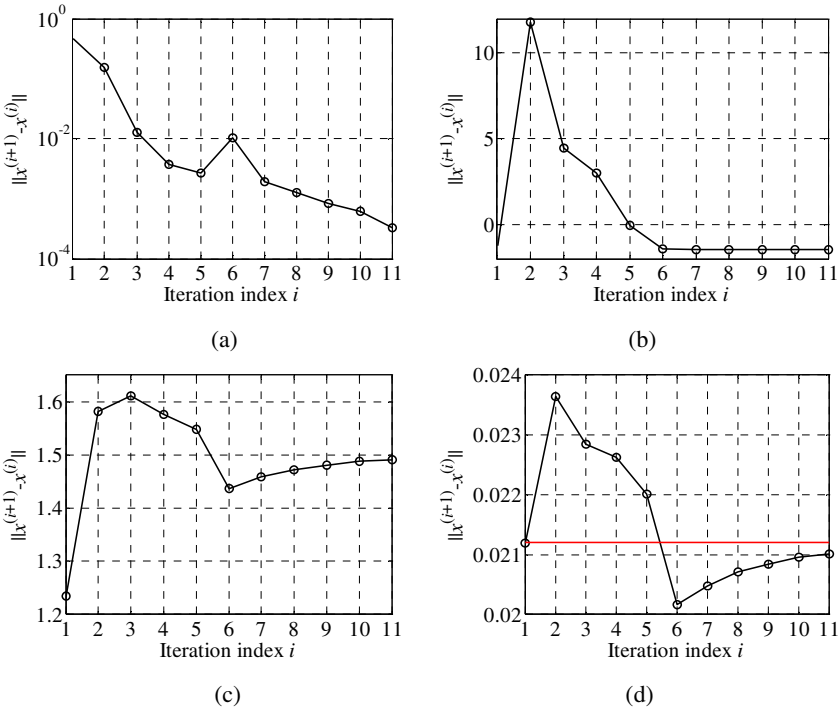

Fig. 4.17 Optimization history; (a) convergence plot; (b) evolution of the objective function; (c) evolution of the lift coefficient; and (d) evolution of the drag coefficient (drag constraint marked using a solid horizontal line). The graphs show all high-fidelity function evaluations performed in the optimization.

4.6 Summary

A variable-fidelity airfoil design optimization algorithm has been presented. The algorithm uses a computationally cheap low-fidelity model to construct a surrogate of an accurate but CPU-intensive high-fidelity model. The low-fidelity model is corrected by aligning the airfoil surface pressure distribution with the corresponding distribution of the high-fidelity model by means of the shape-preserving response correction prediction technique. This ensures a good generalization capability of the surrogate model with respect to both objectives and constraints. The robustness of the algorithm is enhanced by embedding it in the trust region framework. Applications for transonic and high-lift airfoil design are demonstrated with the optimized designs obtained at the computational cost corresponding to of a few high-fidelity model evaluations.

References

1. Hicks, R.M., Henne, P.: A Wing design by numerical optimization. Journal of Aircraft 15(7), 407–412 (1978)
2. Jameson, A.: Aerodynamic design via control theory. Journal of Scientific Computing 3, 233–260 (1988)
3. Reuther, J., Jameson, A.: Control theory based airfoil design for potential flow and a finitie volume discretization. AIAA Paper 94-0499, AIAA 32nd Aerospace Sciences Meeting and Exhibit, Reno, Nevada (1994)
4. Jameson, A., Reuther, J.: Control theory based airfoil design using euler equations. In: Proceedings of AIAA/USAF/NASA/ISSMO Symposium on Multidisciplinary Analsysis and Optimization, Panama City Beach, pp. 206–222 (1994)
5. Kim, S., Alonso, J.J., Jameson, A.: Design optimization of high-lift configurations using a viscous continuous adjoint method. AIAA 40th Aerospace Sciences Meeting & Exhibit, AIAA paper 2002–0844 (2002)
6. Leoviriyakit, K., Kim, S., Jameson, A.: Viscous aerodynamic shape opptimization of wings including planform variables. In: 21st Applied Aerodynamics Conference, Orlando, Florida (2003)
7. Queipo, N.V., Haftka, R.T., Shyy, W., Goel, T., Vaidyanathan, R., Tucker, P.K.: Surrogate-based analysis and optimization. Progress in Aerospace Sciences 41(1), 1–28 (2005)
8. Forrester, A.I.J., Keane, A.J.: Recent advances in surrogate-based optimization. Progress in Aerospace Sciences 45(1-3), 50–79 (2009)
9. Simpson, T.W., Peplinski, J., Koch, P.N., Allen, J.K.: Metamodels for computer-based engineering design: survey and recommendations. Engineering with Computers 17(2), 129–150 (2001)
10. Alexandrov, N.M., Nielsen, E.J., Lewis, R.M., Anderson, W.K.: First-order model management with variable-fidelity physics applied to multi-element airfoil optimization. In: 8th AIAA/USAF/NASA/ISSMO Symposium on Multidisciplinary Design and Optimization, Long Beach, CA, AIAA Paper 2000–4886 (2000)
11. Alexandrov, N.M., Lewis, R.M., Gumbert, C.R., Green, L.L., Newman, P.A.: Optimization with variable-fidelity models applied to wing design. In: 38th Aerospace Sciences Meeting & Exhibit, Reno, NV, AIAA Paper 2000–2841 (2000)
12. Forrester, A.I.J., Bressloff, N.W., Keane, A.J.: Optimization using surrogate models and partially converged computationally fluid dynamics simulations. Proceedings of the Royal Society A: Mathematical, Physical and Engineering Sciences 462(2071), 2177–2204 (2006)
13. Alexandrov, N.M., Lewis, R.M.: An overview of first-order model management for engineering optimization. Optimization and Engineering 2(4), 413–430 (2001)
14. Bandler, J.W., Cheng, Q.S., Dakroury, S.A., Mohamed, A.S., Bakr, M.H., Madsen, K., Søndergaard, J.: Space mapping: the state of the art. IEEE Trans. Microwave Theory Tech. 52(1), 337–361 (2004)
15. Koziel, S., Leifsson, L.: Multi-fidelity high-lift aerodynamic optimization of single-element airfoils. In: Int. Conf. Engineering Optimization, Lisbon (2010)
16. Leifsson, L., Koziel, S.: Multi-fidelity design optimization of transonic airfoils using physics-based surrogate modeling and shape-preserving response prediction. Journal of Computational Science 1(2), 98–106 (2010)

17. Koziel, S., Leifsson, L.: Multi-fidelity high-lift aerodynamic optimization of single-element airfoils. Int. Conf. Engineering Optimization, Lisbon (2010)
18. Koziel, S.: Shape-preserving response prediction for microwave design optimization. IEEE Trans. Microwave Theory and Tech. 58(11), 2829–2837 (2010)
19. ICEM CFD, ver. 12.1, ANSYS Inc., Southpointe, 275 Technology Drive, Canonsburg, PA 15317 (2006)
20. FLUENT.ver. 6.3.26, ANSYS Inc., Southpointe, 275 Technology Drive, Canonsburg, PA 15317 (2006)
21. Murman, E.M., Bailey, F.R., Johnson, M.L.: TSFOIL – A computer code for the two-dimensional transonic calculations, including wind-tunnel wall effects and wave-drag evaluation. In: NASA SP-347, Part II, pp. 769–788 (1975)
22. Koziel, S.: Multi-fidelity multi-grid design optimization of planar microwave structures with Sonnet. In: International Review of Progress in Applied Computational Electromagnetics, Tampere, Finland, pp. 719–724 (2010)
23. Conn, A.R., Gould, N.I.M., Toint, P.L.: Trust Region Methods. MPS-SIAM Series on Optimization (2000)
24. Koziel, S., Bandler, J.W., Madsen, K.: Space-mapping based interpolation for engineering optimization. IEEE Trans. Microwave Theory and Tech. 54(6), 2410–2421 (2006)
25. Spalart, P.R., Allmaras, S.R.: A one-equation turbulence model for aerodynamic flows. In: 30th AIAA Aerospace Sciences Meeting and Exhibit, Reno, Nevada (1992)
26. Koziel, S., Yang, X.-S. (eds.): Computational optimization, methods and algorithms, 1st edn. Springer, Heidelberg (2010)